Electric Power Systems Research 224 (2023) 109680

Contents lists available at ScienceDirect

Electric Power Systems Research

journal homepage: www.elsevier.com/locate/epsr

# Optimal control of a DC microgrid with busbar matrix for high power EV charging☆

Jan Engelhardt [a,*], Samuele Grillo [b], Lisa Calearo [a,c], Marco Agostini [d], Massimiliano Coppo [d], Mattia Marinelli [a]

[a] Department of Wind and Energy Systems, Technical University of Denmark, Roskilde, Denmark
[b] Dipartimento di Elettronica, Informazione e Bioingegneria, Politecnico di Milano, Milan, Italy
[c] Rambøll Danmark A/S, Copenhagen, Denmark
[d] Department of Industrial Engineering, Padova University, Padova, Italy

ARTICLE INFO

*Keywords:*
BESS
Electric vehicles
Fast charging
Reconfigurable battery
Self-consumption
Self-sufficiency

ABSTRACT

Recent advances in the development of reconfigurable batteries pave the way for novel DC microgrid architectures that eliminate the need for DC–DC converters. The present study is focused on the control of a microgrid comprising a battery system with three reconfigurable strings to flexibly operate two electric vehicle (EV) fast chargers, a photovoltaic (PV) system, and a grid-tie inverter. The primary control tasks are to dynamically connect the individual battery strings to the other system components through a busbar matrix, and to manage the energy exchange with the AC grid. The paper formulates the control tasks as a mixed-integer linear optimization problem, virtually splitting the system into three parallel representations, each constructing the perspective of one battery string on the busbar matrix. The functionality of the proposed control is assessed through simulation scenarios using actual PV production and EV charging data of a prototype installed on the Danish island of Bornholm. To quantify the performance, the optimizer is compared with a heuristic control. Considering grid energy costs and revenues through EV charging, the optimal control increased the profit by 5.4% in the summer and 13.0% in the winter scenario, with respect to the benchmark control.

## 1. Introduction

Batteries are expected to play a key role in future power systems. As an energy storage with fast response time and high power capability they qualify for various applications, such as electric vehicles (EV) [1] or stationary storage systems for supporting the electricity network [2,3]. The increasing number of EVs requires the development of sufficient charging infrastructure to fulfill charging needs and mitigate typical concerns of potential customers, such as range anxiety and long charging times [4,5]. In particular, fast chargers of above 50 kW are important assets in locations where short charging times are required, for instance along high ways or in city centers [6]. However, high power charging processes can stress distribution grids [7,8], which makes the deployment of fast chargers dependent on the local grid conditions.

One solution is to equip fast charging stations with stationary battery storage [9]. The battery serves as a power and energy buffer, which allows to install charging stations in places where reinforcing the existing grid infrastructure entails long-term planning or high investment costs [10,11]. Energy storage further facilitates the local usage of renewable energy resources, such as wind and solar, and make the charging station to a certain degree self-sufficient [12]. Thus, the connection of renewables, battery energy storage systems (BESS), and EV chargers in hybrid systems offers the opportunity for a green and grid-friendly future mobility. Conventionally, the different system components have diverse operating voltages and are therefore integrated via DC–DC converters to a common bus [13]. In this microgrid design, the power converters have the key task to convert the voltage levels of the individual units to the bus voltage, and to actively control the power flow to and from the bus [14,15].

However, recent developments in battery designs pave the way for novel microgrid layouts that are fundamentally different from conventional architectures. Based on the need of solving cell unbalance issues, the concept of reconfigurable batteries has emerged in the past years [16,17]. Reconfigurable batteries can change the topology in

☆ This work has received funding from the European H2020 project InsulaE under the Grant Agreement No. 824433, and from the IFD funded TOPChargE project under the Grant Agreement No. 9090-00035A.

* Corresponding author.
*E-mail address:* janen@dtu.dk (J. Engelhardt).

https://doi.org/10.1016/j.epsr.2023.109680
Received 6 October 2022; Accepted 2 July 2023
Available online 24 July 2023

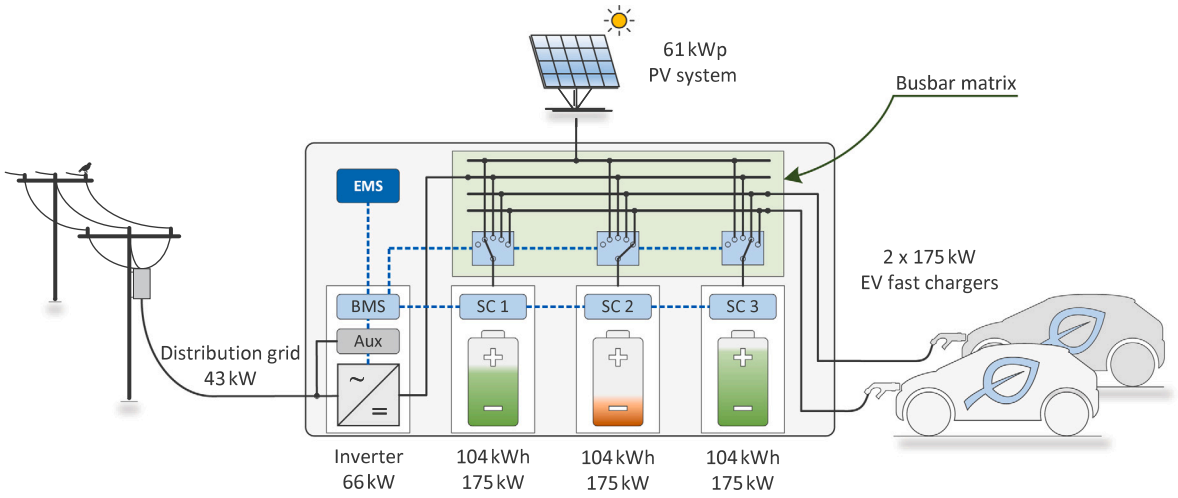


**Fig. 1.** Overview of the DC microgrid comprising three reconfigurable battery strings, a grid-tie inverter, a PV system, and two EV fast chargers. The battery strings are directly connected to the other units through a busbar matrix.
*Source:* Adapted from [22].

which their cells are connected, making it possible to engage and bypass individual cells [18]. Hence, each cell is utilized based on its individual performance, which may increase reliability, lifetime and effective capacity of the whole battery system. Furthermore, the achieved flexibility allows to change the battery voltage dynamically during operation [19]. Recent studies have shown that this capability enables reconfigurable batteries to be directly connected to other DC components and actively control the power flow, without interfacing power converters [20,21].

The H2020 project Insulae explores the potential application of such reconfigurable batteries in battery-buffered EV fast charging stations with local renewable generation [22]. As part of the demonstration activities, a microgrid protopype has been installed on the Danish island of Bornholm [23]. The microgrid design is free of any DC–DC converters and relies fully on the controllability provided by the advanced battery technology. The system comprises three reconfigurable battery strings, two EV fast chargers, a PV system, and a grid-tie inverter. The battery strings can be individually connected to the other components through a busbar matrix, which serves as the central port for directing power flows to and from the storage unit. The prototype is operational and demonstrates the general functionality of this novel microgrid design with reconfigurable battery technology. The energy management system (EMS) of the system, responsible for allocating the components through the busbar matrix and for managing the energy exchange with the grid, is based on heuristic algorithms and applies primary control principles.

In future systems and commercial applications, control algorithms based on optimization have the potential to incorporate all objectives of the different components and unleash the full potential of this new system design. While control concepts for conventional DC microgrid designs have been previously presented in the literature, these cannot be applied to the new system due to its fundamentally different layout. For the microgrid design at hand, no optimal control has been developed or explored in the literature to date. The present study breaks fresh ground by formulating the control tasks as an optimization problem and has the following main contributions:

- The paper proposes an optimal control approach of a DC microgrid with three reconfigurable battery strings and busbar matrix, operated as a fast charging station for electric vehicles accommodating PV generation.
- The methodology applies a virtual system split into three parallel representations, each constructing the perspective of one battery string and converting the busbar matrix into a single point of connection. This allows to seamlessly adapt the formulation for systems with diverse numbers of battery strings.
- The proposed control is tested in a simulation environment with actual PV and EV data, recorded at a demosite on the Danish island of Bornholm where a prototype of the system is installed.
- The performance of the control approach is quantified through various metrics and compared against a benchmark algorithm.

The remainder of the paper is structured as follows: Section 2 introduces the microgrid layout. Section 3 formulates the optimization problem for the control of the system. Section 4 describes the simulation model that was used to test the developed control. Section 5 summarizes and discusses the numerical results, followed by concluding remarks in Section 6.

## 2. Microgrid layout

The system at hand comprises a 312 kWh BESS, two 175 kW EV fast chargers, a 61 kWp PV system, and a 66 kW grid-tied inverter. A high level overview of the setup is provided in Fig. 1. The BESS forms the core of the DC microgrid and consists of three strings with reconfigurable topology. In the following, the term “string” is exclusively used for the battery and no other system component. One string consists of 324 lithium-iron phosphate (LFP) cells with a nominal capacity of 100 Ah and a nominal cell voltage of 3.2 V, resulting in a total string energy capacity of 104 kWh. Each cell can be switched in and out of the series connection, making it possible to dynamically change the string voltage during operation [21]. Hence, each string can be directly connected to another DC component without the need of interfacing power converters.

This facilitates a new system design, where all DC–DC converters are eliminated from the DC microgrid. Instead, the components are connected through a busbar matrix, serving as the central port for power flows within the system. Since the battery strings are the only components with fully controllable voltage range (0–1000 V), the following set of connection rules is defined for the busbar matrix:

- PV system, EV chargers, and inverter can only be connected to battery strings and not among each other.
- Battery strings can only be connected to one other component (PV, EV, inverter) at a time.
- Battery strings cannot be connected among each other.

Each of the strings is equipped with a string controller, which manages the cell configuration to meet the voltage requirements of the connected component. Relevant system states, such as the state of energy (SOE) of the string, are transmitted to the battery management system (BMS). The BMS is the central control unit of the BESS responsible for ensuring safe operation of the system and can disconnect strings if they are operated outside their safe operating area. In the present setup, the battery strings are operated within 10% and 90% of their energy capacity, in order to prevent over- and undercharging. The functionality of the battery string design has been demonstrated through a prototype, which is currently operating on the Danish island of Bornholm [24]. In the following it is therefore assumed that low-level control aspects such as voltage compatibility between the microgrid components are successfully accomplished by the BMS.

The energy management system (EMS) is responsible for managing the energy level of the three strings and has two primary control tasks. Firstly, it assigns the battery strings to the other components, following the connection rules of the busbar matrix. Secondly, it plans and controls the energy exchange with the distribution grid by proposing the power setpoint of the inverter. The following Section describes how the EMS control tasks for such a microgrid design are formulated as an optimization problem.

## 3. Optimization problem

This Section formulates the optimization problem. First, the operating task of allocating units through the busbar matrix is tackled by virtually splitting the microgrid into three parallel representations, each constructing the perspective of one of the three battery strings. Second, the constraints for the external components (PV system, EV chargers, inverter) are defined. Third, the equations defining the operation of battery strings are introduced. Finally, the objective function is formulated. Table 1 summarizes decision variables, parameters, sets, and scalars.

### 3.1. Virtual system split

The busbar matrix allows for each battery string to be connected to one other component at a time (inverter, EV, PV). Hence, the system can be seen from the perspective of each string individually. This is done by splitting the system virtually into three parallel systems, as shown in Fig. 2. Each system represents the perspective of one of the strings while disregarding the remaining strings, and is subject to the busbar constraints summarized in Section 2. The general power balance equation for a string $\zeta$ at each time instance $t$ is given by

$$P^{\mathrm{PV}}_{\zeta,t} + P^{\mathrm{batt,dis}}_{\zeta,t} = P^{\mathrm{ch1}}_{\zeta,t} + P^{\mathrm{ch2}}_{\zeta,t} + P^{\mathrm{batt,ch}}_{\zeta,t} + P^{\mathrm{inv,dc}}_{\zeta,t}, \tag{1}$$

where the left side of the equation summarizes power flows going into the busbar matrix, and the right side power flows going out. Specifically, $P^{\mathrm{PV}}_{\zeta,t}$ is the PV power at time $t$, $P^{\mathrm{batt,dis}}_{\zeta,t}$ is the string discharging power, $P^{\mathrm{ch1}}_{\zeta,t}$ is the charging power for charger 1, $P^{\mathrm{ch2}}_{\zeta,t}$ is the charging power to charger 2, $P^{\mathrm{batt,ch}}_{\zeta,t}$ is the string charging power, and $P^{\mathrm{inv,dc}}_{\zeta,t}$ is the power on the DC side of the inverter. Since the busbar matrix allows for the battery string to be connected to only one component at a time, binary variables are introduced, each defining the connection state between the string and the respective component. For instance, $\gamma^{\mathrm{PV}}_{\zeta,t}$ is '1' if string $\zeta$ is connected to the PV system at time $t$, and '0' if not. Similarly, $\gamma^{\mathrm{ch1}}_{\zeta,t}$, $\gamma^{\mathrm{ch2}}_{\zeta,t}$, and $\gamma^{\mathrm{inv}}_{\zeta,t}$, define the connection state to charger 1, charger 2, and the inverter, respectively. The variables are constrained by

$$\gamma^{\mathrm{ch1}}_{\zeta,t} + \gamma^{\mathrm{ch2}}_{\zeta,t} + \gamma^{\mathrm{inv}}_{\zeta,t} + \gamma^{\mathrm{PV}}_{\zeta,t} \leq 1, \tag{2}$$

as each battery string can only be connected to one other component at a time. The three representations of the system are linked through the following coupling constraints:

$$\sum_{\zeta\in S} \gamma^{\mathrm{PV}}_{\zeta,t} \leq 1, \qquad \sum_{\zeta\in S} \gamma^{\mathrm{ch1}}_{\zeta,t} \leq 1, \tag{3a,b}$$

$$\sum_{\zeta\in S} \gamma^{\mathrm{ch2}}_{\zeta,t} \leq 1, \qquad \sum_{\zeta\in S} \gamma^{\mathrm{inv}}_{\zeta,t} \leq 1. \tag{3c,d}$$

**Table 1**
Nomenclature for decision variables, parameters, and scalars.

| | Value | Unit | Description |
|---|---|---|---|
| **Sets** | | | |
| $t \in T$ | $\in \mathcal{T}$ | h | Set of time instances. |
| $\zeta \in S$ | $\in \mathbb{N}^+$ | – | Set of battery strings. |
| $*$ | – | – | Superscript that stands for ch1/ch2/PV/inv. |
| **Variables** | | | |
| $E^{\mathrm{batt}}_{\zeta,t}$ | $\in \mathbb{R}^+_0$ | kWh | Energy of string $\zeta$. |
| $\epsilon^{\mathrm{batt,up}}_{\zeta,t}$ | $\in \mathbb{R}^+_0$ | kWh | Energy difference to upper SOE threshold. |
| $\epsilon^{\mathrm{batt,low}}_{\zeta,t}$ | $\in \mathbb{R}^+_0$ | kWh | Energy difference to lower SOE threshold. |
| $P^{\mathrm{batt,ch}}_{\zeta,t}$ | $\in \mathbb{R}^+_0$ | kW | Charging power of string $\zeta$. |
| $P^{\mathrm{batt,dis}}_{\zeta,t}$ | $\in \mathbb{R}^+_0$ | kW | Discharging power of string $\zeta$. |
| $P^{\mathrm{inv,dc}}_{\zeta,t}$ | $\in \mathbb{R}$ | kW | DC inverter power of string $\zeta$. |
| $P^{\mathrm{inv,ex,ac}}_{\zeta,t}$ | $\in \mathbb{R}^+_0$ | kW | Export AC inverter power from string $\zeta$. |
| $P^{\mathrm{inv,im,ac}}_{\zeta,t}$ | $\in \mathbb{R}^+_0$ | kW | Import AC inverter power from string $\zeta$. |
| $P^{\mathrm{PV}}_{\zeta,t}$ | $\in \mathbb{R}^+_0$ | kW | PV power to string $\zeta$. |
| $P^{\mathrm{ch1}}_{\zeta,t}$ | $\in \mathbb{R}^+_0$ | kW | Power for charger 1 provided by string $\zeta$. |
| $P^{\mathrm{ch2}}_{\zeta,t}$ | $\in \mathbb{R}^+_0$ | kW | Power for charger 2 provided by string $\zeta$. |
| $\rho^{\mathrm{inv,ex}}_{\zeta,t}$ | $\in \mathbb{R}^+_0$ | kW | Increase in inverter export power. |
| $\rho^{\mathrm{inv,im}}_{\zeta,t}$ | $\in \mathbb{R}^+_0$ | kW | Increase in inverter import power. |
| $\Psi^{\mathrm{sw}}_t$ | $\in \mathbb{R}^+_0$ | € | Switching costs. |
| $\Psi^{\mathrm{PV}}_t$ | $\in \mathbb{R}^+_0$ | € | PV curtailment costs. |
| $\Psi^{\mathrm{EV}}_t$ | $\in \mathbb{R}^+_0$ | € | Costs for not delivered EV energy. |
| $\Psi^{\mathrm{batt}}_t$ | $\in \mathbb{R}^+_0$ | € | Costs for exceeding SOE thresholds. |
| $\Psi^{\mathrm{inv}}_t$ | $\in \mathbb{R}^+_0$ | € | Costs for inverter setpoint changes. |
| $\alpha^{\mathrm{inv}}_{\zeta,t}$ | $\in [0, 1]$ | – | Inverter status: import (0), export (1). |
| $\beta^{\mathrm{batt}}_{\zeta,t}$ | $\in [0, 1]$ | – | String status: charging (0), disch. (1). |
| $\delta^{*}_{\zeta,t}$ | $\in [0, 1]$ | – | String status: '1' if getting disconn. from *. |
| $\gamma^{*}_{\zeta,t}$ | $\in [0, 1]$ | – | Status of $\zeta$ and *: disconn. (0), conn. (1). |
| **Parameters** | | | |
| $P^{\mathrm{ch1}}_t$ | $\in \mathbb{R}^+_0$ | kW | Power request at EV charger 1. |
| $P^{\mathrm{ch2}}_t$ | $\in \mathbb{R}^+_0$ | kW | Power request at EV charger 2. |
| $P^{\mathrm{PV}}_t$ | $\in \mathbb{R}^+_0$ | kW | Available PV power. |
| $\pi^{\mathrm{inv,im}}_t$ | $\in \mathbb{R}$ | € | Import electricity price. |
| $\pi^{\mathrm{inv,ex}}_t$ | $\in \mathbb{R}$ | € | Export electricity price. |
| **Scalars** | | | |
| $\Delta t$ | $\in \mathbb{R}^+_0$ | h | Time step of optimization intervals. |
| $\eta^{\mathrm{inv}}$ | $\in \mathbb{R}^+_0$ | – | Constant fraction of inverter efficiency. |
| $\eta^{\mathrm{batt}}$ | $\in \mathbb{R}^+_0$ | – | Constant battery string efficiency. |
| $E^{\mathrm{batt}}_{\mathrm{max}}$ | $\in \mathbb{R}^+_0$ | kWh | Upper energy limit of battery string. |
| $E^{\mathrm{batt}}_{\mathrm{min}}$ | $\in \mathbb{R}^+_0$ | kWh | Lower energy limit of battery string. |
| $E^{\mathrm{batt}}_{\mathrm{pen,up}}$ | $\in \mathbb{R}^+_0$ | kWh | Upper threshold for SOE penalty. |
| $E^{\mathrm{batt}}_{\mathrm{pen,low}}$ | $\in \mathbb{R}^+_0$ | kWh | Lower threshold for SOE penalty. |
| $P^{\mathrm{inv}}_{\mathrm{loss,con}}$ | $\in \mathbb{R}^+_0$ | kW | Constant fraction of inverter losses. |
| $P^{\mathrm{batt}}_{\mathrm{max}}$ | $\in \mathbb{R}^+_0$ | kW | Maximum absolute power of battery string. |
| $P^{\mathrm{inv,im}}_{\mathrm{max}}$ | $\in \mathbb{R}^+_0$ | kW | Maximum import power at grid connection. |
| $P^{\mathrm{inv,ex}}_{\mathrm{max}}$ | $\in \mathbb{R}^+_0$ | kW | Maximum export power at grid connection. |
| $\xi^{\mathrm{PV}}$ | $\in \mathbb{R}^+_0$ | €/kWh | Penalty for curtailing PV energy. |
| $\xi^{\mathrm{EV}}$ | $\in \mathbb{R}^+_0$ | €/kWh | Penalty for not delivering requested EV energy. |
| $\xi^{\mathrm{inv}}$ | $\in \mathbb{R}^+_0$ | €/kW | Penalty for changing inverter setpoint. |
| $\xi^{\mathrm{sw},*}$ | $\in \mathbb{R}^+_0$ | € | Penalty for switching battery string. |
| $\xi^{\mathrm{batt,up}}$ | $\in \mathbb{R}^+_0$ | €/kWh | Penalty for exceeding upper SOE threshold. |
| $\xi^{\mathrm{batt,low}}$ | $\in \mathbb{R}^+_0$ | €/kWh | Penalty for exceeding lower SOE threshold. |

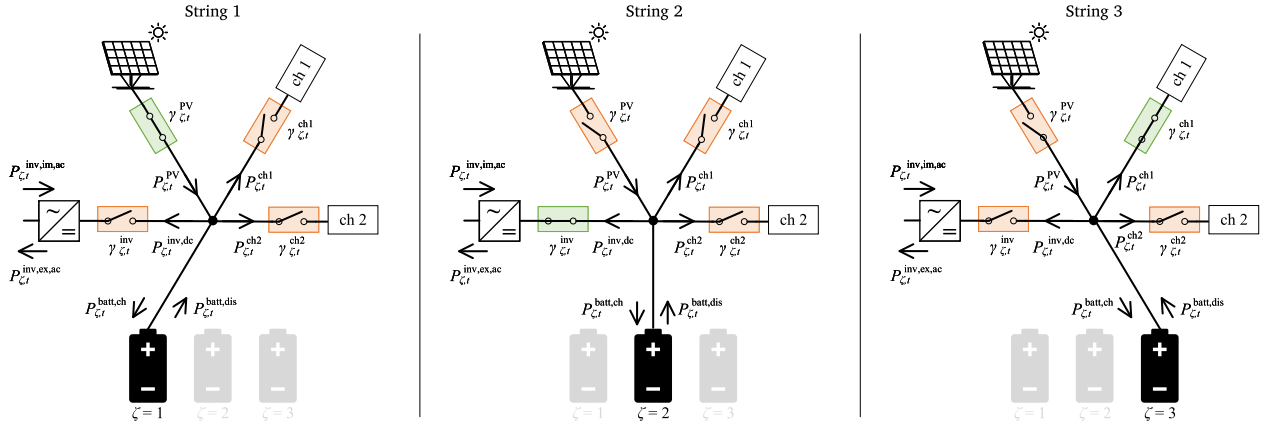


**Fig. 2.** Virtual system split into three parallel representations. Each representation constructs the perspective of one of three battery strings, converting the busbar matrix into a single connection point to which the external components are linked.

These constraints are imposed by the busbar matrix and make sure that only one string is connected to the same components at the same time. Additional binary variables $\delta^{*}_{\zeta,t}$ are introduced to specify if at time $t$, string $\zeta$ gets disconnected from unit $*$ (EV chargers, PV, inverter):

$$\delta^{\mathrm{PV}}_{\zeta,t} \geq \gamma^{\mathrm{PV}}_{\zeta,(t-1)} - \gamma^{\mathrm{PV}}_{\zeta,t}, \qquad \delta^{\mathrm{ch1}}_{\zeta,t} \geq \gamma^{\mathrm{ch1}}_{\zeta,(t-1)} - \gamma^{\mathrm{ch1}}_{\zeta,t}, \tag{4a,b}$$

$$\delta^{\mathrm{ch2}}_{\zeta,t} \geq \gamma^{\mathrm{ch2}}_{\zeta,(t-1)} - \gamma^{\mathrm{ch2}}_{\zeta,t}, \qquad \delta^{\mathrm{inv}}_{\zeta,t} \geq \gamma^{\mathrm{inv}}_{\zeta,(t-1)} - \gamma^{\mathrm{inv}}_{\zeta,t}. \tag{4c,d}$$

These variables allow for setting a price $\Psi^{\mathrm{sw}}_{t}$ for switching actions to avoid unnecessary switching between the strings and the other components:

$$\Psi^{\mathrm{sw}}_{t} = \sum_{\zeta \in S} \left( \xi^{\mathrm{sw,ch}} \cdot (\delta^{\mathrm{ch1}}_{\zeta,t} + \delta^{\mathrm{ch2}}_{\zeta,t}) + \xi^{\mathrm{sw,inv}} \cdot \delta^{\mathrm{inv}}_{\zeta,t} + \xi^{\mathrm{sw,PV}} \cdot \delta^{\mathrm{PV}}_{\zeta,t} \right), \tag{5}$$

where $\xi^{\mathrm{sw,ch}}$, $\xi^{\mathrm{sw,inv}}$, $\xi^{\mathrm{sw,PV}}$ are penalization costs for EV chargers, inverter, and PV system, respectively. Such costs need to be set according to the characteristics of each component and according to the strategy that the optimizer needs to pursue. The setting of such terms is discussed in relation to the case study further in the paper. The connection state variables $\gamma^{*}_{\zeta,t}$ further allow to put constraints on the power flow between the strings and the individual components, as described in the following subsection.

### 3.2. PV system, EV chargers, and inverter

The available PV power $P^{\mathrm{PV}}_{t}$ can only flow to string $\zeta$, if the two units are connected through the busbar matrix. Hence, the constraints for the actual PV power to the string are defined by

$$0 \leq P^{\mathrm{PV}}_{\zeta,t} \leq \gamma^{\mathrm{PV}}_{\zeta,t} \cdot P^{\mathrm{PV}}_{t}. \tag{6}$$

To incentivize the use of local PV production, curtailment of PV energy should be avoided. Hence, a curtailment penalty is defined as

$$\Psi^{\mathrm{PV}}_{t} = \xi^{\mathrm{PV}} \cdot \left( P^{\mathrm{PV}}_{t} - \sum_{\zeta \in S} P^{\mathrm{PV}}_{\zeta,t} \right) \cdot \Delta t, \tag{7}$$

where $\xi^{\mathrm{PV}}$ is a penalization factor defining the costs for curtailed PV energy (€/kWh), and $\Delta t$ is the time step of the optimization.

For EV charging, the power requests at the two chargers, $P^{\mathrm{ch1}}_{t}$ and $P^{\mathrm{ch2}}_{t}$, can only be met if a string is connected to the corresponding charger. Furthermore, a string should only be connected to a charger during the energy transfer to an EV. These constraints are summarized in the following equations:

$$0 \leq P^{\mathrm{ch1}}_{\zeta,t} \leq \gamma^{\mathrm{ch1}}_{\zeta,t} \cdot P^{\mathrm{ch1}}_{t}, \tag{8a}$$

$$0 \leq P^{\mathrm{ch2}}_{\zeta,t} \leq \gamma^{\mathrm{ch2}}_{\zeta,t} \cdot P^{\mathrm{ch2}}_{t}, \tag{8b}$$

$$\gamma^{\mathrm{ch1}}_{\zeta,t} \leq P^{\mathrm{ch1}}_{t}/\mathrm{W}, \tag{8c}$$

$$\gamma^{\mathrm{ch2}}_{\zeta,t} \leq P^{\mathrm{ch2}}_{t}/\mathrm{W}. \tag{8d}$$

A cost $\Psi^{\mathrm{EV}}_{t}$ is introduced that penalizes energy that was requested at the EV chargers, but not delivered. The cost is calculated as

$$\Psi^{\mathrm{EV}}_{t} = \xi^{\mathrm{EV}} \cdot \left( P^{\mathrm{ch1}}_{t} + P^{\mathrm{ch2}}_{t} - \sum_{\zeta \in S} (P^{\mathrm{ch1}}_{\zeta,t} + P^{\mathrm{ch2}}_{\zeta,t}) \right) \cdot \Delta t, \tag{9}$$

where $\xi^{\mathrm{EV}}$ is a penalization factor defining the costs for not delivered EV energy (€/kWh).

In case of the inverter, a distinction is made between the AC and the DC side, to account for the power losses of the component. Furthermore, the bidirectional capability requires to represent the AC power by two parts $P^{\mathrm{inv,ex,ac}}_{\zeta,t}$ and $P^{\mathrm{inv,im,ac}}_{\zeta,t}$, corresponding to grid export and import, respectively. The direction is defined by a binary variable $\alpha^{\mathrm{inv}}_{\zeta,t}$ that is '1' for grid export, and '0' for import. Using the two binary variables $\alpha^{\mathrm{inv}}_{\zeta,t}$ and $\gamma^{\mathrm{inv}}_{\zeta,t}$, the constraints for the AC grid power are summarized by the following equations:

$$0 \leq P^{\mathrm{inv,ex,ac}}_{\zeta,t} \leq \gamma^{\mathrm{inv}}_{\zeta,t} \cdot P^{\mathrm{inv,ex}}_{\max}, \tag{10a}$$

$$0 \leq P^{\mathrm{inv,im,ac}}_{\zeta,t} \leq \gamma^{\mathrm{inv}}_{\zeta,t} \cdot P^{\mathrm{inv,im}}_{\max}, \tag{10b}$$

$$0 \leq P^{\mathrm{inv,ex,ac}}_{\zeta,t} \leq \alpha^{\mathrm{inv}}_{\zeta,t} \cdot P^{\mathrm{inv,ex}}_{\max}, \tag{10c}$$

$$0 \leq P^{\mathrm{inv,im,ac}}_{\zeta,t} \leq (1 - \alpha^{\mathrm{inv}}_{\zeta,t}) \cdot P^{\mathrm{inv,im}}_{\max}. \tag{10d}$$

Eqs. (10a) and (10b) ensure that energy exchange with the grid only occurs if the inverter is connected to the string, and Eqs. (10c) and (10d) ensure that it is either exported or imported. The power losses of the inverter are modeled with two parts. Firstly, a loss fraction with linear dependency on the inverter power is considered through a constant efficiency $\eta^{\mathrm{inv}}$. Secondly, constant losses $P^{\mathrm{inv}}_{\mathrm{loss,con}}$ through inverter auxiliary systems occur when the inverter is active. Hence, the relation between AC and DC power of the inverter is given by

$$P^{\mathrm{inv,dc}}_{\zeta,t} = \frac{P^{\mathrm{inv,ex,ac}}_{\zeta,t}}{\eta^{\mathrm{inv}}} - P^{\mathrm{inv,im,ac}}_{\zeta,t} \cdot \eta^{\mathrm{inv}} + \gamma^{\mathrm{inv}}_{\zeta,t} \cdot P^{\mathrm{inv}}_{\mathrm{loss,con}}. \tag{11}$$

More information on the inverter efficiency model is presented in Section 4. To reduce the impact of the microgrid on the AC distribution grid, a cost $\Psi^{\mathrm{inv}}_{t}$ for increasing the inverter power setpoint is defined:

$$\Psi^{\mathrm{inv}}_{t} = \xi^{\mathrm{inv}} \cdot (\rho^{\mathrm{inv,ex}}_{\zeta,t} + \rho^{\mathrm{inv,im}}_{\zeta,t}), \tag{12a}$$

$$\rho^{\mathrm{inv,ex}}_{t} \geq \sum_{\zeta \in S} (P^{\mathrm{inv,ex,ac}}_{\zeta,t} - P^{\mathrm{inv,ex,ac}}_{\zeta,(t-1)}), \tag{12b}$$

$$\rho^{\mathrm{inv,im}}_{t} \geq \sum_{\zeta \in S} (P^{\mathrm{inv,im,ac}}_{\zeta,t} - P^{\mathrm{inv,im,ac}}_{\zeta,(t-1)}), \tag{12c}$$

where $\rho^{\mathrm{inv,ex}}_{t}$ and $\rho^{\mathrm{inv,im}}_{t}$ (kW) are increases in the inverter power setpoint for grid export and import, respectively, and the parameter $\xi^{\mathrm{inv}}$

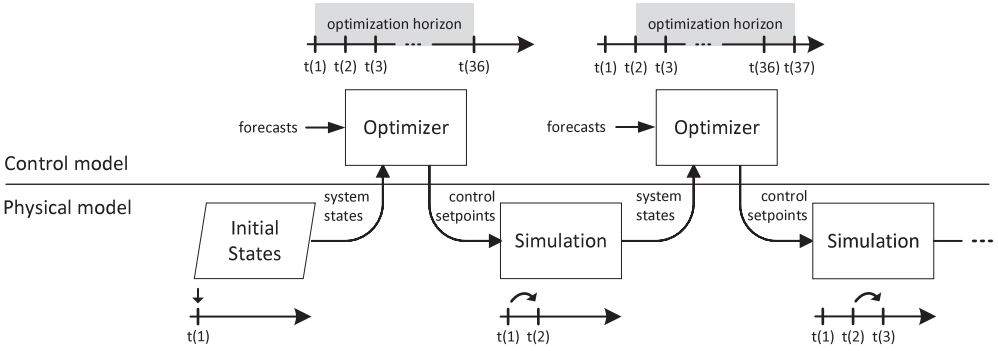


**Fig. 3.** Overview of the simulation structure for testing the control model.

is a penalization factor defining the costs for power increase (€/kW) linked to the user's grid connection fees.

### 3.3. Battery strings

As for the inverter, the battery string power has two possible directions, represented by the binary variable $\beta^{\text{batt}}_{\zeta,t}$. The variable takes the value '0' for charging, and '1' for discharging. Charging is only possible if the battery string is connected to either the PV system or the inverter, while discharging is only possible if the string is connected to one of the two chargers or the inverter. This is being ensured by the following constraints:

$$1 - \beta^{\text{batt}}_{\zeta,t} \leq \gamma^{\text{PV}}_{\zeta,t} + \gamma^{\text{inv}}_{\zeta,t}, \tag{13a}$$

$$\beta^{\text{batt}}_{\zeta,t} \leq \gamma^{\text{ch1}}_{\zeta,t} + \gamma^{\text{ch2}}_{\zeta,t} + \gamma^{\text{inv}}_{\zeta,t}. \tag{13b}$$

The string power is composed of two separate components for charging and discharging. Since both are mutually exclusive at the same time instance $t$, $\beta^{\text{batt}}_{\zeta,t}$ is used to constrain their upper limit through

$$0 \leq P^{\text{batt,ch}}_{\zeta,t} \leq (1 - \beta^{\text{batt}}_{\zeta,t}) \cdot P^{\text{batt}}_{\text{max}}, \tag{14a}$$

$$0 \leq P^{\text{batt,dis}}_{\zeta,t} \leq \beta^{\text{batt}}_{\zeta,t} \cdot P^{\text{batt}}_{\text{max}}, \tag{14b}$$

where $P^{\text{batt,ch}}_{\zeta,t}$ and $P^{\text{batt,dis}}_{\zeta,t}$ are charging and discharging power, respectively. The energy stored in a battery string is defined by the following constraints:

$$E^{\text{batt}}_{\text{min}} \leq E^{\text{batt}}_{\zeta,t} \leq E^{\text{batt}}_{\text{max}}, \tag{15a}$$

$$E^{\text{batt}}_{\zeta,t} = E^{\text{batt}}_{\zeta,(t-1)} - \left( \frac{P^{\text{batt,dis}}_{\zeta,t}}{\eta^{\text{batt}}} - P^{\text{batt,ch}}_{\zeta,t} \cdot \eta^{\text{batt}} \right) \Delta t, \tag{15b}$$

where $E^{\text{batt}}_{\text{min}}$ and $E^{\text{batt}}_{\text{max}}$ are the minimum and maximum string energy, respectively, $\eta^{\text{batt}}$ is the string efficiency, and $\Delta t$ is the time step of the optimization.

A cost $\Psi^{\text{batt}}_{t}$ is introduced when operating the battery system close to its maximum and minimum energy limits. Continuously operating the battery close to its maximum energy limit accelerates battery degradation. Conversely, if the battery has a low charge level and more EVs arrive than predicted, those vehicles could not be charged. For this reason, upper and lower energy limits $E^{\text{batt}}_{\text{pen,up}}$ and $E^{\text{batt}}_{\text{pen,low}}$ are introduced. When crossing these limits, penalization factors $\xi^{\text{batt,up}}$ and $\xi^{\text{batt,low}}$ (€/kWh/h) apply to the energy difference above the upper limit $\epsilon^{\text{batt,up}}_{\zeta,t}$ or below the lower limit $\epsilon^{\text{batt,up}}_{\zeta,t}$, respectively. The battery energy level costs are summarized in the following equations:

$$\Psi^{\text{batt}}_{t} = (\xi^{\text{batt,up}} \cdot \epsilon^{\text{batt,up}}_{\zeta,t} + \xi^{\text{batt,low}} \cdot \epsilon^{\text{batt,up}}_{\zeta,t}) \cdot \Delta t, \tag{16a}$$

$$\epsilon^{\text{batt,up}}_{\zeta,t} >= \sum_{\zeta \in S} E^{\text{batt}}_{\zeta,t} - E^{\text{batt}}_{\text{pen,up}}, \tag{16b}$$

$$\epsilon^{\text{batt,low}}_{\zeta,t} >= E^{\text{batt}}_{\text{pen,low}} - \sum_{\zeta \in S} E^{\text{batt}}_{\zeta,t}. \tag{16c}$$

### 3.4. Objective function

The objective function $J$ addresses multiple control aspects and is formulated as a minimization problem with regard to the set of decision variables ($D.V.$). The goals are to minimize the grid energy costs (import costs minus revenues from export), and the penalization costs for PV, EV, inverter, and the battery system:

$$\begin{aligned} \min_{D.V.} J = \sum_{t \in T} \Big( & \big( \pi^{\text{inv,im}}_{t} \cdot \sum_{\zeta \in S} P^{\text{inv,im,ac}}_{\zeta,t} \\ & - \pi^{\text{inv,ex}}_{t} \cdot \sum_{\zeta \in S} P^{\text{inv,ex,ac}}_{\zeta,t} \big) \cdot \Delta t \\ & + \Psi^{\text{sw}}_{t} + \Psi^{\text{PV}}_{t} + \Psi^{\text{EV}}_{t} + \Psi^{\text{inv}}_{t} + \Psi^{\text{batt}}_{t} \Big), \end{aligned} \tag{17}$$

where $\pi^{\text{inv,im}}_{t}$ and $\pi^{\text{inv,ex}}_{t}$ are the electricity prices (€/kWh) for importing and exporting energy from/to the grid, respectively. The different penalization factors $\xi^{*}$ can be set to prioritize specific control goals. This will be further addressed in Section 4.3.

## 4. Simulation model

This Section describes the simulation environment that is used to test the proposed optimization algorithm. First, the simulation structure is presented. Then, the data used to create the test scenarios are introduced. Finally, the parameter settings of the optimization are defined.

### 4.1. Simulation structure

The performance of the proposed optimization is assessed in a simulation environment using the tools Matlab & Simulink [25] and CPLEX [26]. Fig. 3 provides an overview of the simulation structure. A mathematical model of the microgrid developed in Matlab & Simulink was adopted from a previous work [22]. This physical model represents the characteristics and dynamic states of the microgrid components. The CPLEX optimizer is integrated into the simulation environment and acts as the EMS of the system. As such, it is called in intervals of $\Delta t$ = 5 min and provided with the current system states, as well as with a 3 h rolling forecast for expected EV charging demand, PV production, and electricity prices. When called, the optimizer calculates the setpoints for busbar matrix and inverter power in intervals of $\Delta t$ = 5 min for the 3 h horizon, and returns the proposed setpoints to the physical system. The physical model applies the setpoints and simulates the next 5 min. The system states after this interval may be different than predicted, for instance due to inaccuracies in the forecast. Hence, the optimizer is called again with updated system states and forecasts to re-evaluate the setpoints for busbar matrix and inverter. As depicted in Fig. 3, this procedure is repeated throughout the simulation.

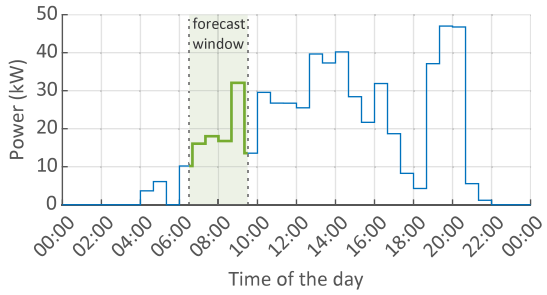


**Fig. 4.** Generic daily EV forecast pattern used to create a 3 h rolling forecast of EV charging.

### 4.2. Input data

EV charging data are available from the demosite on Bornholm, where the prototype is operated. All charging events recorded between June 2021 and March 2022 were filtered to only consider sessions with a charged energy of at least 10 kWh and an average charging power of above 40 kW. The remaining 102 charging sessions were sorted by their respective arrival time – day of the week and time of the day – to create a 7-day timeseries of charging requests at the two EV chargers. A queue management algorithm was applied to assign arriving EVs to the chargers depending on their availability. In case both chargers were occupied, arriving EVs queued to be recharged.

To challenge the developed optimization algorithm with unforeseen charging events, the exact arrival time of the vehicles remains concealed to the EMS. Instead, a generic forecast profile was created, where the charging request of all days was averaged in intervals of 40 min. Fig. 4 shows this EV consumption pattern, which is used to provide a rolling 3 h forecast horizon for the optimizer. It is assumed that when an EV connects to one of the chargers, the optimizer is informed about charging duration and energy request of this specific charging session.

For the PV system, actual production data from the microgrid were used to create two different scenarios with different levels of PV power. The first timeseries was recorded from June 1st–7th, 2021, and represents a period with high PV potential, while the second timeseries was recorded from November 1st–7th, 2021, representing a period with low PV potential. The electricity prices for imported and exported energy were considered with historical values for the same periods as the PV data. The electricity prices comprise the hourly intraday price [27], TSO tariffs, and DSO tariffs. TSO tariffs [28] for imported energy include system tariffs ("Systemtarif"), grid tariffs ("Nettarif"), and balancing tariffs for consumption ("Balancetarif for forbrug"), and for exported energy feed-in tariffs ("Indfødningstarif") and balancing tariffs for production ("Balancetarif for produktion"). DSO tariffs arise only for imported energy and are dependent on the time of the day, the day of the week, and the season, as further specified in [29].

### 4.3. Optimizer settings

Table 2 summarizes the optimizer settings in the simulation model. As mentioned in Section 3.4, the penalty costs can be set to prioritize specific control goals. In the presented use case, EV charging has the highest priority, as it is the service provided to the customers and the main source of profit. Hence, the penalty of 10 €/kWh for not delivering energy requested by the EVs is based on the value of lost load (VoLL) for private end users [30]. Similarly, the penalty for PV curtailment of 0.1 €/kWh is based on the levelized cost of energy (LCOE) of rooftop PV system [31]. The costs of 0.02 €/kW for changing the inverter setpoint incentivize grid-friendly operation with a constant progression of the inverter power. Yet, the value is low enough to allow a full step up to the available grid capacity (0.86 €) when the battery needs to be recharged through the grid in periods with high EV utilization. The switching costs for disconnecting battery strings from other components are set in descending order from chargers, inverter, to PV system, to avoid switching strings during charging sessions and preferably use inverter and PV system to achieve the desired overall charge level. The upper SOE penalization $\xi^{\text{batt,up}}$, applied when the total battery SOE exceeds 70%, considers the increasing calendar degradation of LFP cells between 70% and 90%. Based on [32], the degradation was estimated as $1.5 \cdot 10^{-5}$ %/h for each percent that the upper SOE threshold is exceeded. Considering a battery cost of 550 €/kWh [33], the upper SOE penalization was calculated as 0.0017 €/kWh/h. Furthermore, the penalization cost of 0.1 €/kWh/h when the system's SOE drops below 40% was set above the average grid export price of 0.08 €/kWh, and ensures that the optimizer aims at maintaining a certain energy buffer for unforeseen charging events. The remaining parameters presented in Table 2 are directed at the respective component properties of inverter and battery strings, as introduced in Sections 3.2 and 3.3.

**Table 2**
Optimizer settings in the simulation model.

| | Scalar | Value |
|---|---|---|
| Penalization | $\xi^{\text{EV}}$ | 10 €/kWh |
| | $\xi^{\text{PV}}$ | 0.1 €/kWh |
| | $\xi^{\text{inv}}$ | 0.02 €/kW |
| | $\xi^{\text{sw,ch}}$ | 1 € |
| | $\xi^{\text{sw,inv}}$ | 0.5 € |
| | $\xi^{\text{sw,PV}}$ | 0.25 € |
| | $\xi^{\text{batt,up}}$ | 0.0017 €/kWh/h |
| | $\xi^{\text{batt,low}}$ | 0.1 €/kWh/h |
| Battery | $E^{\text{batt}}_{\text{max}}$ | $85\,\% \cdot E^{\text{batt}}_{\text{N}}$ |
| | $E^{\text{batt}}_{\text{min}}$ | $15\,\% \cdot E^{\text{batt}}_{\text{N}}$ |
| | $E^{\text{batt}}_{\text{pen,up}}$ | $70\,\% \cdot 3E^{\text{batt}}_{\text{N}}$ |
| | $E^{\text{batt}}_{\text{pen,low}}$ | $40\,\% \cdot 3E^{\text{batt}}_{\text{N}}$ |
| | $\eta^{\text{batt}}$ | 92.5 % |
| Inverter | $\eta^{\text{inv}}$ | 98.35 % |
| | $P^{\text{inv}}_{\text{loss,con}}$ | 111 W |
| | $P^{\text{inv,ex}}_{\text{max}}$ | 43 kW |
| | $P^{\text{inv,im}}_{\text{max}}$ | 39.5 kW |

## 5. Results and discussion

This Section presents the results obtained from the simulation runs. First, the functionality of the proposed control is discussed for the summer scenario. Second, the results of the winter scenario are shown. Finally, the results from both scenarios are quantified through a set of metrics, and compared with the results achieved by a benchmark control.

### 5.1. Summer week

The first scenario covers the simulation of a summer week with actual PV production data from June 1st–7th, 2021. Fig. 5 shows a representative excerpt of this simulation of two of the days, June 4th and 5th. It can be seen that the trend of the available PV power shows clear differences between the two days. While June 4th shows an intermittent production profile due to cloud coverage, June 5th offers a relatively smooth progression of the available PV power. The requested power at the two fast chargers is significantly higher compared to the PV system, ranging between 45 kW and 160 kW for the shown time period. In this regard, please note the different $y$-axis scaling of the two upper subplots. The EV consumption forecast provides the optimizer with a certain degree of preparation for periods in which

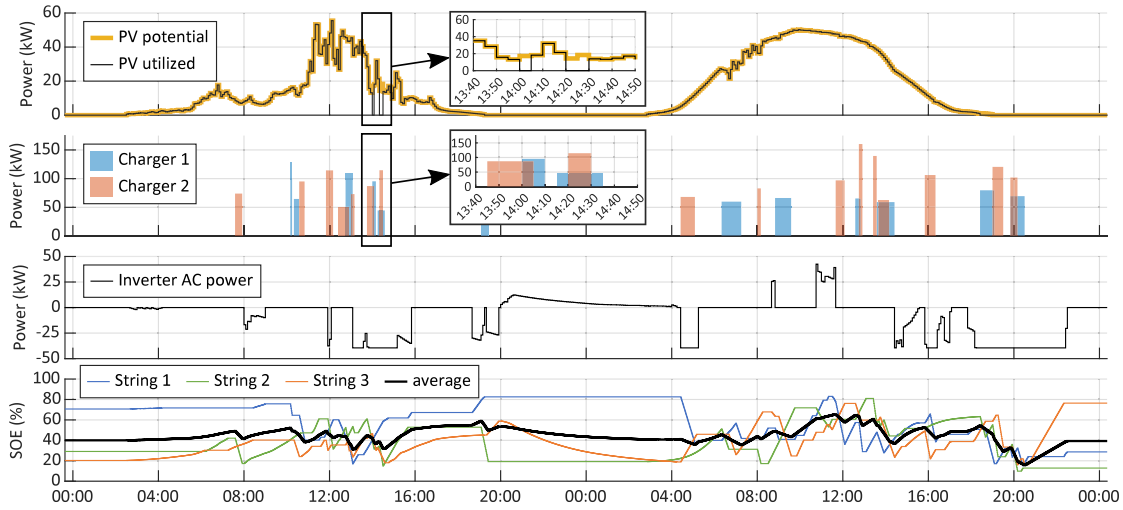


**Fig. 5.** Excerpt of two representative days, June 4th and 5th, from the simulated summer scenario.

higher energy demand is expected. However, as in real life applications, the actual charging request remain unknown to the chargers until the EVs connect. The progression of the inverter power is presented in the third subplot, with positive values corresponding to export and negative values corresponding to import. It can be seen that in the shown period more energy is imported than exported. The last subplot shows the SOE for the three battery strings, as well as the average value representing the system SOE. Due to the penalization on system SOE values of below 40%, the optimizer usually keeps the charge level above this level. However, periods with intense EV charging can bring the charge level below 40%. In such situations, the inverter imports energy from the grid to restore the SOE. Conversely, when the power consumption through EVs is expected to be low, the inverter is used to generate revenues by exporting energy to the grid. This is apparent during the night from June 4th to 5th, where String 3 is discharged from 59% to 19%, causing the system SOE to approach 40%. Another key moment occurs at 14:00 on June 4th, when PV energy is curtailed. At this moment, an EV arrives at Charger 1 in addition to the EV already charging at Charger 2. As a response to the rapidly dropping system SOE, the optimizer disconnects String 3 from the PV system and connects it to the inverter instead which provides a higher import power than the PV potential at this time. PV power is resumed directly when the EV at Charger 2 disconnects, allowing to assign String 2 to the PV system. A similar situation occurs 15 min later, with the PV curtailment lasting for 10 min.

### 5.2. Winter week

The second scenario covers the simulation of a winter week, using data from November 1st–7th, 2021. Fig. 6 shows a representative excerpt of two of the days, November 1st and 2nd. Compared with the first scenario, the PV potential is significantly lower, both in terms of peak power and total energy. Consequently, the grid exchange is characterized by notable grid import in order to meet the EV demand. Grid export is only performed when the expected EV consumption is low and the storage charge level sufficiently high. The buffering effect of the battery storage on the grid is apparent when comparing the power profiles of the inverter and the two EV chargers. The grid exchange is characterized by periods with constant power, while the EV charging pattern is intermittent and at significantly higher power levels ranging from 51 kW up to 128 kW on these two days. Furthermore, the battery allows to cover EV demand with local PV production even when the coincidence factor between the units is low, as on November 1st. On this winter day, the available PV energy allows to increase the average battery SOE from 59% to 72%, until the EVs arriving from 11:40 lead to a successive decrease of the charge level. As in the summer scenario, the penalty on SOE values below 40% incentivizes the optimizer to increase the inverter setpoint in periods where the charge level drops below this value. This provides an important energy buffer for periods where the energy demand from EVs is unexpectedly high. For instance, the six charging sessions after 19:45 on November 2nd required 117 kWh, which is 2.5 times of what the EV forecast assumed for this period. Consequently, the inverter is used to restore the charge level back to 40% which allows to meet unforeseen charging events in the upcoming hours.

### 5.3. Comparative analysis

The results of the 1-week simulations are further quantified through several key metrics summarized in Table 3, to assess the performance of the proposed control in the two scenarios. The metrics are categorized in groups related to EV charging, PV system, grid exchange, and economical considerations. For EV charging, the delivered energy of all 102 charging sessions is compared with the energy requested by the EVs. Since both the summer and the winter scenario are simulated with the same 1-week EV charging pattern, the requested energy is the same in both cases. The charging system controlled by the optimizer managed to fulfill the EV demand with 99.8% and 98.2% in the summer and winter scenario, respectively. For the PV system, the values of available and utilized energy are compared. One difference between the two scenarios is the significant contrast in available energy, with the summer week offering a more than ten times higher PV potential than the winter week. From the available PV energy, the optimizer utilized 99% in the summer scenario, and 92.1% in the winter scenario. The grid exchange is characterized by a higher import than export in both seasons, yet, with different shares. While in the simulated summer week the exported energy was around half of the imported energy, in the winter week 58 kWh exported energy compares against 2.9 MWh imported energy. Another important metric is the self-sufficiency of the system, which states what percentage of the consumed EV energy was provided by the local PV system. The calculations were based on [34], and gave values of 69% for the summer week, and 6% for the winter week. The accumulated energy costs for the grid exchange are negative in both seasons, since generally more energy is imported than exported. In winter, the loss is around 5 times higher than in summer, due to the higher energy import and almost no export. However, the grid energy costs are relatively small compared to the revenues generated through EV charging, calculated based on charging costs of 0.8 €/kWh. All in

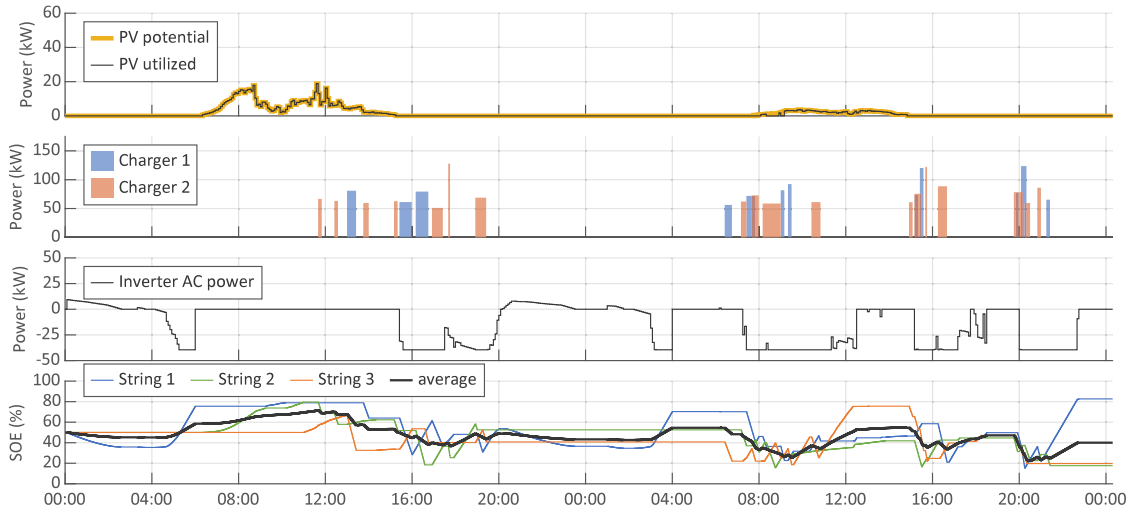


**Fig. 6.** Excerpt of two representative days, November 1st and 2nd, from the simulated winter scenario.

**Table 3**
Summary of simulation results for summer and winter scenario, and comparison to benchmark algorithm.

| Category | Metric | Optimization | | Heuristic control [22] | |
|---|---|---|---|---|---|
| | | Summer week | Winter week | Summer week | Winter week |
| EV charging | Requested energy | 2766 kWh | 2766 kWh | 2766 kWh | 2766 kWh |
| | Delivered energy | 2761 kWh | 2718 kWh | 2622 kWh | 2428 kWh |
| | Ratio | 99.8% | 98.2% | 94.8% | 87.8% |
| PV system | Available energy | 2546 kWh | 239 kWh | 2546 kWh | 239 kWh |
| | Utilized energy | 2520 kWh | 220 kWh | 2546 kWh | 239 kWh |
| | Ratio | 99% | 92.1% | 100% | 100% |
| Grid exchange | Exported energy | 548 kWh | 58 kWh | 824 kWh | 29 kWh |
| | Imported energy | 1157 kWh | 2914 kWh | 1921 kWh | 2541 kWh |
| | Self-sufficiency [34] | 69% | 6% | 57% | 9% |
| Economics | Grid energy costs | 76 € | 396 € | 75 € | 369 € |
| | Revenues EV charging | 2208 € | 2174 € | 2097 € | 1943 € |
| | Total profit | 2132 € | 1778 € | 2022 € | 1574 € |

all, the slightly higher delivered EV energy together with lower grid energy costs make the simulated summer week more profitable than the winter week.

To compare the performance of the proposed optimization against a benchmark, a heuristic control algorithm from a previous study [22] was tested with the same scenarios. The results were assessed with the same metrics and are also summarized in Table 3. While the heuristic control utilizes all the available PV energy in both scenarios, it performs worse in EV charging. In the summer week, 94.8% of the requested energy at the EV chargers was delivered, while in the winter week this value was 87.8%. This highlights the strength of the optimizer, which weights the different objectives against each other and, for instance, curtails PV energy if the solar potential is low during intervals of high EV utilization. This becomes particularly apparent in the winter scenario, where the optimizer curtailed around 8% of the available PV energy to allow for reliable EV charging. Furthermore, the optimizer achieves a higher self-sufficiency despite the curtailed PV energy, since generally more energy is delivered to the EVs. In the economical comparison, the difference in grid energy costs are marginal. However, the higher revenues through EV charging make the optimizer the more profitable management system, increasing the profit by 5.4% in the summer and 13.0% in the winter scenario, with respect to the benchmark control.

## 6. Conclusion

The present study proposes an energy management system based on optimization for controlling a DC microgrid with busbar matrix and modular battery storage. The presented system design comprises three reconfigurable battery strings, which can be directly connected to other DC components through a busbar matrix, without the need of interfacing DC–DC converters. The main tasks of the management system is to dynamically assign the individual battery strings to the other system components, namely two EV fast-chargers, a PV system, and a grid connected inverter, and to control the power exchange with the primary grid. The proposed MILP optimization performs a virtual system split into three separate representations, where each subsystem is considering the busbar matrix from the perspective of one single battery string. The three system representations are linked through coupling constraints imposing the connection rules of the busbar matrix.

The performance of the control approach was assessed in a simulation environment consisting of a Matlab&Simulink model of the physical system, with integrated CPLEX optimizer for solving the optimization problem. The test scenarios were based on PV production patterns and EV charging behavior at an actual prototype of this new microgrid design. The simulations demonstrated the functionality of the proposed control method. To quantify the performance, the optimizer was compared with a heuristic control, which was tested with the same scenarios. While the benchmark control fully utilized the available PV energy, the proposed optimization algorithm curtailed PV energy during periods of low solar potential and high EV demand. By utilizing the grid connection instead to recharge the battery strings, the optimal control provided an important energy buffer for intervals with unexpectedly high EV charging. Hence, the optimizer was able to deliver on average 99.0% of the total energy requested by all EVs, while

the heuristic control achieved 91.3%. Taking into account grid energy costs and revenues through EV charging, the optimal control method increased the profit by 5.4% in the summer and 13.0% in the winter scenario, with respect to the benchmark control.

## Declaration of competing interest

The authors declare that they have no known competing financial interests or personal relationships that could have appeared to influence the work reported in this paper.

## Data availability

The data that has been used is confidential.

## References


[1] R. Fachrizal, M. Shepero, D. van der Meer, J. Munkhammar, J. Widén, Smart charging of electric vehicles considering photovoltaic power production and electricity consumption: A review, eTransportation 4 (2020) http://dx.doi.org/10.1016/j.etran.2020.100056.

[2] D. Choi, N. Shamim, A. Crawford, Q. Huang, C.K. Vartanian, V.V. Viswanathan, M.D. Paiss, M.J.E. Alam, D.M. Reed, V.L. Sprenkle, Li-ion battery technology for grid application, J. Power Sources 511 (July) (2021) 230419, http://dx.doi.org/10.1016/j.jpowsour.2021.230419.

[3] M. Ahmadi, O.B. Adewuyi, M.S.S. Danish, P. Mandal, A. Yona, T. Senjyu, Optimum coordination of centralized and distributed renewable power generation incorporating battery storage system into the electric distribution network, Int. J. Electr. Power Energy Syst. 125 (June 2020) (2021) 106458, http://dx.doi.org/10.1016/j.ijepes.2020.106458.

[4] Q. Zhang, H. Li, L. Zhu, P.E. Campana, H. Lu, F. Wallin, Q. Sun, Factors influencing the economics of public charging infrastructures for EV – A review, Renew. Sustain. Energy Rev. 94 (June) (2018) 500–509, http://dx.doi.org/10.1016/j.rser.2018.06.022.

[5] C. Brand, C. Cluzel, J. Anable, Modeling the uptake of plug-in vehicles in a heterogeneous car market using a consumer segmentation approach, Transp. Res. A 97 (2017) 121–136, http://dx.doi.org/10.1016/j.tra.2017.01.017.

[6] R. Wolbertus, R. Van den Hoed, Electric vehicle fast charging needs in cities and along corridors, World Electr. Veh. J. 10 (2) (2019) 1–13, http://dx.doi.org/10.3390/wevj10020045.

[7] L. Wang, Z. Qin, T. Slangen, P. Bauer, T. Van Wijk, Grid Impact of Electric Vehicle Fast Charging Stations: Trends, Standards, Issues and Mitigation Measures - An Overview, IEEE Open J. Power Electron. 2 (January) (2021) 56–74, http://dx.doi.org/10.1109/OJPEL.2021.3054601.

[8] C.H. Dharmakeerthi, N. Mithulananthan, T.K. Saha, Impact of electric vehicle fast charging on power system voltage stability, Int. J. Electr. Power Energy Syst. 57 (2014) 241–249, http://dx.doi.org/10.1016/j.ijepes.2013.12.005.

[9] M.M. Mahfouz, M.R. Iravani, Grid-integration of battery-enabled DC fast charging station for electric vehicles, IEEE Trans. Energy Convers. 35 (1) (2020) 375–385, http://dx.doi.org/10.1109/TEC.2019.2945293.

[10] T. Unterluggauer, J. Rich, P.B. Andersen, S. Hashemi, Electric vehicle charging infrastructure planning for integrated transportation and power distribution networks: A review, eTransportation 12 (2022) 100163, http://dx.doi.org/10.1016/j.etran.2022.100163.

[11] L. Calearo, A. Thingvad, C. Ziras, M. Marinelli, A methodology to model and validate electro-thermal-aging dynamics of electric vehicle battery packs, J. Energy Storage 55 (May) (2022).

[12] O. Hafez, K. Bhattacharya, Optimal design of electric vehicle charging stations considering various energy resources, Renew. Energy 107 (2017) 576–589, http://dx.doi.org/10.1016/j.renene.2017.01.066.

[13] V.T. Tran, M.R. Islam, K.M. Muttaqi, D. Sutanto, An efficient energy management approach for a solar-powered EV battery charging facility to support distribution grids, IEEE Trans. Ind. Appl. 55 (6) (2019) 6517–6526, http://dx.doi.org/10.1109/TIA.2019.2940923.

[14] D. Sbordone, I. Bertini, B. Di Pietra, M.C. Falvo, A. Genovese, L. Martirano, EV fast charging stations and energy storage technologies: A real implementation in the smart micro grid paradigm, Electr. Power Syst. Res. 120 (2015) 96–108, http://dx.doi.org/10.1016/j.epsr.2014.07.033.

[15] G. Sharma, V.K. Sood, M.S. Alam, S.M. Shariff, Comparison of common DC and AC bus architectures for EV fast charging stations and impact on power quality, eTransportation 5 (2020) 100066, http://dx.doi.org/10.1016/j.etran.2020.100066.

[16] S. Ci, N. Lin, D. Wu, Reconfigurable battery techniques and systems: A survey, IEEE Access 4 (2016) 1175–1189, http://dx.doi.org/10.1109/ACCESS.2016.2545338.

[17] S. Muhammad, M. Usman Rafique, S. Li, Z. Shao, Q. Wang, X. Liu, Reconfigurable battery systems: A survey on hardware architecture and research challenges, ACM Trans. Des. Autom. Electron. Syst. 24 (2) (2019) http://dx.doi.org/10.1145/3301301.

[18] Z. Wei, J. Zhao, H. He, G. Ding, H. Cui, L. Liu, Future smart battery and management: Advanced sensing from external to embedded multi-dimensional measurement, J. Power Sources 489 (December 2020) (2021) 229462, http://dx.doi.org/10.1016/j.jpowsour.2021.229462.

[19] J. Engelhardt, J.M. Zepter, T. Gabderakhmanova, M. Marinelli, Efficiency Characteristic of a High-Power Reconfigurable Battery with Series-Connected Topology, in: 2022 International Power Electronics Conference, IPEC-Himeji 2022-ECCE Asia, IEEJ-IAS, 2022, pp. 2370–2376, http://dx.doi.org/10.23919/IPEC-Himeji2022-ECCE53331.2022.9807176.

[20] J. Engelhardt, T. Gabderakhmanova, G. Rohde, M. Marinelli, Reconfigurable stationary battery with adaptive cell switching for electric vehicle fast-charging, in: UPEC 2020 - 2020 55th International Universities Power Engineering Conference, Proceedings, 2020, http://dx.doi.org/10.1109/UPEC49904.2020.9209774.

[21] J. Engelhardt, J.M. Zepter, T. Gabderakhmanova, G. Rohde, M. Marinelli, Double-string battery system with reconfigurable cell topology operated as a fast charging station for electric vehicles, Energies 14 (9) (2021) http://dx.doi.org/10.3390/en14092414, URL https://www.mdpi.com/1996-1073/14/9/2414.

[22] J. Engelhardt, J.M. Zepter, T. Gabderakhmanova, M. Marinelli, Energy management of a multi-battery system for renewable-based high power EV charging, eTransportation 14 (March) (2022) 100198, http://dx.doi.org/10.1016/j.etran.2022.100198, arXiv:2112.00351.

[23] T. Gabderakhmanova, J. Engelhardt, J.M. Zepter, T.M. Sorensen, K. Boesgaard, H.H. Ipsen, M. Marinelli, Demonstrations of DC microgrid and virtual power plant technologies on the Danish Island of Bornholm, in: UPEC 2020 - 2020 55th International Universities Power Engineering Conference, Proceedings, 2020, http://dx.doi.org/10.1109/UPEC49904.2020.9209853.

[24] A. Bowen, J. Engelhardt, T. Gabderakhmanova, M. Marinelli, Battery buffered EV fast chargers on Bornholm: Charging patterns and grid integration, in: Proceedings of the 57th International Universities Power Engineering Conference, 2022.

[25] MATLAB, version 9.10.0 (R2021a), The MathWorks Inc., Natick, Massachusetts, 2021.

[26] Cplex IBM ILOG, V12.10: User's Manual for CPLEX, International Business Machines Corporation, 2019.

[27] Nord Pool AS, Nord pool intraday statistics, 2021, URL https://www.nordpoolgroup.com/Market-data1/Intraday/Market-data1/Market-data1/Overview/?dd=DK2&view=table.

[28] Energinet, Energinets tariffer for el dækker omkostninger til drift, afskrivninger, finansiering og administration, 2021, URL https://energinet.dk/El/Elmarkedet/Tariffer/Aktuelle-tariffer (Accessed on 5 December 2021).

[29] Radius, Radius' priser siden 2012, 2021, URL https://radiuselnet.dk/wp-content/uploads/El_Radius_Priser_siden_2011.pdf (Accessed on 10 December 2021).

[30] T. Schröder, W. Kuckshinrichs, Value of lost load: An efficient economic indicator for power supply security? A literature review, Front. Energy Res. 3 (DEC) (2015) 1–12, http://dx.doi.org/10.3389/fenrg.2015.00055.

[31] C. Kost, T. Schlegl, J. Thomsen, S. Nold, J. Mayer, N. Hartmann, C. Senkpiel, S. Philipps, S. Lude, N. Saad, Fraunhofer ISE: Levelized cost of electricity - renewable energy technologies, march 2018, Fraunhofer ISE: Lev. Cost Electr. Renew. Energy Technol. (March) (2018) 25.

[32] P. Keil, S.F. Schuster, J. Wilhelm, J. Travi, A. Hauser, R.C. Karl, A. Jossen, Calendar aging of lithium-ion batteries, J. Electrochem. Soc. 163 (9) (2016) A1872–A1880, http://dx.doi.org/10.1149/2.0411609jes.

[33] CATL, CATL Energy Storage System Solutions and Product Brochure. URL https://www.catl.com/en/ess/ (Accessed on 10 August 2022).

[34] J.M. Zepter, J. Engelhardt, T. Gabderakhmanova, M. Marinelli, Re-thinking the definition of self-sufficiency in systems with energy storage, in: Proceedings of 2022 International Conference on Smart Energy Systems and Technologies Publication, 2022, URL http://insulae-h2020.eu.